

## THE ORIGINS OF UV-OPTICAL COLOR GRADIENTS IN STAR-FORMING GALAXIES AT $z \sim 2$ : PREDOMINANT DUST GRADIENTS BUT NEGLIGIBLE sSFR GRADIENTS

F. S. LIU <sup>†,1,2</sup>, DONGFEI JIANG,<sup>1,3</sup> S. M. FABER,<sup>2</sup> DAVID C. KOO,<sup>2</sup> HASEN M. YESUF,<sup>2</sup> SANDRO TACCHELLA,<sup>4</sup>  
SHUDE MAO,<sup>5,6,7</sup> WEICHEN WANG,<sup>8</sup> YICHENG GUO,<sup>2</sup> JEROME J. FANG,<sup>2,9</sup> GUILLERMO BARRO,<sup>2,10</sup> XIANZHONG ZHENG,<sup>3,11</sup>  
MENG JIA,<sup>1</sup> WEI TONG,<sup>1</sup> LU LIU,<sup>1</sup> AND XIANMIN MENG<sup>6</sup>

<sup>1</sup>College of Physical Science and Technology, Shenyang Normal University, Shenyang 110034, China

<sup>2</sup>University of California Observatories and the Department of Astronomy and Astrophysics, University of California, Santa Cruz, CA 95064, USA

<sup>3</sup>Purple Mountain Observatory, Chinese Academy of Sciences, 2 West-Beijing Road, Nanjing 210008, China

<sup>4</sup>Department of Physics, Institute for Astronomy, ETH Zurich, CH-8093 Zurich, Switzerland

<sup>5</sup>Physics Department and Tsinghua Centre for Astrophysics, Tsinghua University, Beijing 100084, China

<sup>6</sup>National Astronomical Observatories, Chinese Academy of Sciences, A20 Datun Road, Beijing 100012, China

<sup>7</sup>Jodrell Bank Centre for Astrophysics, School of Physics and Astronomy, The University of Manchester, Oxford Road, Manchester M13 9PL, UK

<sup>8</sup>Department of Physics & Astronomy, Johns Hopkins University, 3400 N. Charles Street, Baltimore, MD 21218, USA

<sup>9</sup>Orange Coast College, Costa Mesa, CA 92626, USA

<sup>10</sup>Department of Astronomy, University of California, Berkeley, CA 94720-3411, USA

<sup>11</sup>Chinese Academy of Sciences South America Center for Astronomy, China-Chile Joint Center for Astronomy, Camino El Observatorio 1515, Las Condes, Santiago, Chile

### ABSTRACT

The rest-frame UV-optical (i.e.,  $NUV - B$ ) color is sensitive to both low-level recent star formation (specific star formation rate - sSFR) and dust. In this Letter, we extend our previous work on the origins of  $NUV - B$  color gradients in star-forming galaxies (SFGs) at  $z \sim 1$  to those at  $z \sim 2$ . We use a sample of 1335 large (semi-major axis radius  $R_{\text{SMA}} > 0.''18$ ) SFGs with extended UV emission out to  $2R_{\text{SMA}}$  in the mass range  $M_* = 10^9 - 10^{11} M_\odot$  at  $1.5 < z < 2.8$  in the CANDELS/GOODS-S and UDS fields. We show that these SFGs generally have negative  $NUV - B$  color gradients (redder centers), and their color gradients strongly increase with galaxy mass. We also show that the global rest-frame  $FUV - NUV$  color is approximately linear with  $A_V$ , which is derived by modeling the observed integrated FUV to NIR spectral energy distributions of the galaxies. Applying this integrated calibration to our spatially-resolved data, we find a negative dust gradient (more dust extinguished in the centers), which steadily becomes steeper with galaxy mass. We further find that the  $NUV - B$  color gradients become nearly zero after correcting for dust gradients regardless of galaxy mass. This indicates that the sSFR gradients are negligible and dust reddening is likely the principal cause of negative UV-optical color gradients in these SFGs. Our findings support that the buildup of the stellar mass in SFGs at the Cosmic Noon is self-similar inside  $2R_{\text{SMA}}$ .

*Keywords:* galaxies: photometry — galaxies: star formation — galaxies: high-redshift

## 1. INTRODUCTION

Investigating the spatial distribution of star-formation is a powerful way to understand how stellar mass is built up and where the star-formation is shut down in galaxies as they evolve along the star-forming main sequence (SFMS). It has been known that rest-frame UV-optical (i.e.,  $NUV - B$ ) color is sensitive to both low-level recent star formation (i.e., specific star formation rate - sSFR) and dust ( $A_V$ ), but it is insensitive to the metallicity (Kaviraj et al. 2007; Pan et al. 2015). Thus, UV-optical star formation measurements are ambiguous without accurate dust correction, especially for high-redshift star-forming galaxies (SFGs).

Radial sSFR and dust gradients in distant galaxies have not been fully explored to date. There are only few related papers on this topic. By stacking the *HST* multi-band imaging, Wuyts et al. (2012) studied the resolved colors and stellar populations of a few hundred SFGs with  $M_* > 10^{10} M_\odot$  at  $0.5 < z < 2.5$ . They found evidence for redder colors, lower sSFR and increased dust attenuation in the centers of galaxies. Tacchella et al. (2015) used  $H\alpha$  fluxes to measure the sSFR gradients in  $z \sim 2.2$  SFGs. They claimed rather shallow sSFR gradients at low masses ( $M_* < \sim 10^{11} M_\odot$ ) and significant sSFR gradients at  $M_* \sim 10^{11} M_\odot$ . Note that they corrected for dust reddening assuming a flat attenuation profile. In a series of papers, Nelson et al. (2012, 2016a,b) studied the maps of sSFR traced by  $H\alpha$  and of dust in SFGs at moderate redshifts ( $z \sim 1$  and  $z \sim 1.4$ ) by stacking the spatially-resolved spectra of 3D-HST. Nelson et al. (2012) showed that the  $H\alpha$  sizes of massive galaxies are bigger than their rest-frame  $R$ -band sizes. Nelson et al. (2016a) showed that the  $EW(H\alpha)$  is flat with radius for the low-mass ( $M_* = 10^9 - 10^{9.5} M_\odot$ ) galaxies, while it falls by a factor of  $\sim 2$  on average from the center to twice the effective radius for more massive galaxies. These findings suggested that massive SFGs at moderate redshifts buildup their stellar masses from the inside out, while the low-mass SFGs grow in a self-similar way irrespective of the radial distance. Note that dust correction was not done in these two works. Later, Nelson et al. (2016b) corrected the data in their previous papers for dust by using the Balmer decrement ( $H\alpha/H\beta$ ). As a result, central dust was found to be a huge factor in establishing radial colors and sSFR gradients in galaxies with a mean mass of  $\langle M_* \rangle \sim 10^{10.2} M_\odot$ . Galaxies with  $\langle M_* \rangle \sim 10^{9.2} M_\odot$  have little dust attenuation at all radii.

Recently, Liu et al. (2016, hereafter Paper I) used high-resolution *HST* optical-IR imaging (in observed  $B$  through  $H$  band) to measure the rest-frame  $NUV - B$  color gradients in the main-sequence SFGs at  $z \sim 1$ . In

Paper I, after correcting for dust reddening, the radial  $NUV - B$  color gradients were shown to be nearly zero in SFGs with  $M_* < 10^{10} M_\odot$ , but significant residual color gradients were found in SFGs with  $M_* > 10^{10.5} M_\odot$ . Dust gradients were determined by fitting reddened stellar population models to the spatially-resolved spectral energy distributions (SEDs) with FAST (Kriek et al. 2009). These findings implied that at  $z \sim 1$  dust reddening is the principal cause of rest-frame  $NUV - B$  color gradients in low-mass SFGs, while for high-mass SFGs, age gradients are also an important factor. More recently, Wang et al. (2017) expanded our Paper I and re-visited the dust and sSFR gradients in  $z = 0.4 - 1.4$  SFGs on the main-sequence inferred from the  $UVI$  ( $U - V$  versus  $V - I$ ) diagrams. Their conclusion is generally consistent with that of Paper I, except that their estimated central sSFR for massive SFGs are 2-3 times smaller than ours. In this work, we extend our Paper I to  $z \sim 2$  with a sample of 1335 large SFGs with extended UV emission out to twice the semi-major axis radius in the mass range  $M_* = 10^9 - 10^{11} M_\odot$  at  $1.5 < z < 2.8$  in the CANDELS/GOODS-S and UDS fields. We show that the global rest-frame  $FUV - NUV$  color is approximately linear with  $A_V$  and the dust-corrected  $NUV - B$  color is indeed a good tracer of sSFR. Applying these calibrations to our spatially-resolved data, we examine the effects of dust gradients and sSFR gradients on the  $NUV - B$  color gradients in these SFGs at the Cosmic Noon and further discuss their link to the stellar mass assembly.

Throughout the Letter, we adopt a cosmology with a matter density parameter  $\Omega_m = 0.3$ , a cosmological constant  $\Omega_\Lambda = 0.7$  and a Hubble constant of  $H_0 = 70 \text{ km s}^{-1} \text{ Mpc}^{-1}$ . All magnitudes are in the AB system.

## 2. DATA

We select galaxies in our sample from the first two publicly-available fields of the CANDELS. Namely, the Great Observatories Origins Deep Survey (GOODS-S, Guo et al. 2013) and the UKIDSS Ultra-Deep Survey (UDS, Galametz et al. 2013). The CANDELS team has made a multi-wavelength catalog based on source detection in the F160W ( $H$ ) band for each field, combining the newly obtained CANDELS *HST*/WFC3 data with existing public ground-based and space-based data. *HST* photometry was measured by running SExtractor (Bertin & Arnouts 1996) on the point spread function (PSF)-matched images in the dual-image mode, with the F160W image as the detection image. Photometry in ground-based and IRAC images, whose resolutions are much lower than that of the F160W images, was measured with TFIT (Laidler et al. 2007), which fit the

PSF-smoothed high-resolution image templates to the low-resolution images to measure the fluxes in the low-resolution images. We refer readers to Guo et al. (2013) and Galametz et al. (2013) for details on these data and the reduction procedure.

Photometric redshifts were estimated from a variety of different codes available in the literature, which are then combined to improve the individual performance (Dahlen et al. 2013). Rest-frame total magnitudes in various standard filters, from  $FUV$  to  $K$ , were computed using the best available redshifts (spectroscopic or photometric) and multi-wavelength photometry using EAZY (Brammer et al. 2008), which fits a set of galaxy SED templates to the observed photometry. Stellar masses come from the CANDELS official catalog released by Santini et al. (2015), which combine the results from ten separate SED fitting methods. A Chabrier (2003) initial mass function (IMF) is assumed. Semi-major axis radius ( $R_{SMA}$ ) and axis ratio ( $b/a$ ) were measured from the  $HST/WFC3$  F160W images using GALFIT (Peng et al. 2002) by van der Wel et al. (2012). SFRs come from rest-frame  $NUV$  luminosities at  $\lambda \approx 2800\text{\AA}$  that are corrected for extinction by assuming a Calzetti law ( $A_{2800} \approx 1.79A_V$ ):  $SFR_{NUV,cor}[M_{\odot}yr^{-1}] = 2.59 \times 10^{-10} L_{NUV,cor}[L_{\odot}]$  (Kennicutt & Evans 2012). We prefer this approach because of its simplicity and more direct relation to the observed SED. The rates of star-formation derived from a combination of unobscured UV and IR emission ( $SFR_{UV+IR}$ ) are nominally a more faithful measure than  $SFR_{NUV,cor}$ , since it incorporates a *direct* measure of obscured star formation. However,  $L_{IR}$  is usually overestimated in galaxies above  $z \sim 1.5$ , where observed 24  $\mu\text{m}$  probes PAH emission (Tielens 2008). Fitting local IR templates will return a value of  $L_{IR}$  that is systematically too high (Salim et al. 2009). Given the theoretical uncertainties still surrounding the origin of warm dust in galaxies, it is reasonable to adopt the  $NUV-NIR$  SED-fitting rates, as we do here, pending further developments in our understanding of mid-IR galaxy SEDs. The median  $A_V$  was computed by combining results from four methods (labeled  $2a_{\tau}$ ,  $12a$ ,  $13a_{\tau}$  and  $14a$ ) in Santini et al. (2015). The four methods were chosen with the same assumptions (Chabrier IMF and Calzetti extinction law).

The  $HST$  based multi-wavelength and multi-aperture photometry catalogs with improved local background subtraction were built for galaxies in the CANDELS fields (Liu et al. in prep.), which include the radial profiles of observed surface brightness and cumulative magnitude in the  $HST/WFC3$  (F105W, F125W, F140W, and F160W) bands and  $HST/ACS$  (F435W, F606W,

F775W, F814W and F850LP) bands if available. The photometry were performed on the multi-band, PSF-matched images.

### 3. SAMPLE SELECTION

The full GOODS-S and UDS catalogs contain 34,930 and 35,932 objects, respectively. The parent sample used in this work is constructed by applying the following cuts to the above data:

1. Observed F160W( $H$ ) magnitude  $H < 24.5$  and the GALFIT quality flag = 0 in F160W (van der Wel et al. 2012) to ensure well-constrained GALFIT measurements and eliminate doubles, mergers, and disturbed objects.
2. Photometry quality flag PhotFlag = 0 to exclude spurious sources.
3. SExtractor CLASS\_STAR < 0.9 to reduce contamination by stars.
4. Redshifts within  $1.5 < z < 2.8$  for GOODS-S and  $2.2 < z < 2.8$  for UDS to roughly cover rest-frame  $FUV$  to  $B$  simultaneously. Note that the shortest observed band in GOODS-S available is F435W( $B$ ) and the shortest one in UDS is F606W( $V$ ).
5. Stellar masses at  $10^9 < M_{*}/M_{\odot} < 10^{11}$  to maintain  $\sim 90\%$  ( $\sim 75\%$ ) completeness limit at  $z = 1.5$  ( $z = 2.8$ ) for SFGs (van der Wel et al. 2014; Morishita et al. 2015).
6.  $R_{SMA} > 0.18''$  (3 pixels) to minimize the effect of PSF-matching on color gradient measurement.
7. Well-constrained measurements of surface brightness profiles from center to  $2R_{SMA}$  in observed F435W( $B$ ) for  $1.5 < z < 2.2$  in GOODS-S and ones in observed F606W( $V$ ) for  $2.2 < z < 2.8$  in both GOODS-S and UDS to guarantee sample galaxies with extended rest-frame UV emission.

After the cuts 1-5, we obtain 2388 galaxies: 1666 from GOODS-S and 722 from UDS. After the cuts 1-7, we obtain 1430 galaxies in total. We then utilize the rest-frame  $UVJ$  ( $U - V$  versus  $V - J$ ) diagram ( $(U - V) < 0.88 \times (V - J) + 0.49$ , Williams et al. 2009) to select 1405 SFGs (see the left panel in Figure 1). Furthermore, we follow the method used in Paper I to select SFGs near the ridge-line of the SFMS (see the right panel in Figure 1). After excluding 70 transition galaxies, which are defined as galaxies with offsets from the best-fit main-

sequence relation ( $\log sSFR_{\text{NUV,cor}}/\text{yr}^{-1} = -0.25 \pm 0.01 \times \log M_*/M_\odot - 6.20 \pm 0.13$ ) of  $\Delta \log sSFR_{\text{NUV,cor}} < -0.45$  dex (below the dashed line), we focus on 1335 main-sequence SFGs. We note that the majority of very dusty SFGs are excluded by the selection cuts 6 and 7 (see the left panel in Figure 1), which are not probed in this analysis.

#### 4. RESULTS AND ANALYSIS

We investigate the global properties of the sample galaxies to find an accessible and good indicator of dust attenuation ( $A_V$ ) that can be used in our spatially-resolved analysis and check whether rest-frame  $NUV - B$  color is a good tracer of sSFR after removing dust effect. One of the most common methods for dust determination at high redshift is fitting reddened stellar population models to the integrated broad-band SEDs of galaxies (e.g., Kriek et al. 2009). The long-wavelength (i.e., rest-frame  $J$ ) data is usually needed by this method. It has been shown that this method is closely related to the  $UVJ$  method that distinguishes dust reddening from old stars (Patel et al. 2011). Unfortunately, the high-resolution  $HST$  imaging in CANDELS ends at observed  $H$  band, which roughly corresponds to a cut at rest-frame  $B$  to  $V$  for our galaxies. The lack of long-wavelength high-resolution data can not meet the need of distinguishing dust reddening from age in spatially-resolved analysis. Nevertheless, the rest-frame  $FUV - NUV$  color is accessible in both integrated and resolved data, which has been widely applied to evaluate the  $UV$  slope  $\beta$  and thus determine dust attenuation (e.g., Buat et al. 2005; Muñoz-Mateos et al. 2007; Reddy et al. 2012). In the left panel of Figure 2, we show the relation of global  $A_V$  versus rest-frame  $FUV - NUV$  for our SFGs. It can be seen that rest-frame  $FUV - NUV$  color is approximately linear with  $A_V$ . The best linear fit is given as  $A_V = 1.38 \pm 0.02 \times (FUV - NUV) + 0.30 \pm 0.01$ . In the right panel of Figure 2, we show the relation of  $\log sSFR_{\text{NUV,cor}}$  versus  $(NUV - B)_{\text{dc}}$ . The dust correction exploits the median  $A_V$  derived by modeling the observed integrated  $FUV$  to NIR SEDs and assumes a Calzetti law. This plot demonstrates that the dust-corrected  $NUV - B$  color is indeed a good tracer of sSFR for our SFGs. The best polynomial fit to this relation is given as  $\log sSFR_{\text{NUV,cor}}/\text{yr}^{-1} = 0.62 \pm 0.01 \times (NUV - B)_{\text{dc}}^2 - 1.78 \pm 0.02 \times (NUV - B)_{\text{dc}} - 7.88 \pm 0.13$ .

Applying the above calibrations from integrated photometry and SED modeling to our spatially-resolved data, we can infer the radial  $A_V$  gradients and sSFR gradients to disentangle their effects on the  $NUV - B$  color gradients. For this work we computed the rest-

frame  $FUV$ ,  $NUV$  and  $B$  band surface brightness profiles of each sample galaxy using EAZY (Brammer et al. 2008) as well (refer to Figure 2 in Paper I). In Figure 3, we show the raw dust-reddened  $FUV - NUV$  profiles and inferred  $A_V$  profiles, which are normalised by their  $R_{\text{SMA}}$  in arcsec (upper) and are shown in physical radius (lower), respectively. The individual galaxy profiles are shown with gray lines. To quantify the general trends, we used the linear model `lm` function in R programming language to fit a straight line as a mean of the individual profiles between PSF FWHM ( $0.18''$ ) and  $2R_{\text{SMA}}$  in each panel. The best-fit slopes and intercepts are presented in Table 1. The best-fit models with  $2\sigma$  lower and upper limits are shown as shaded regions in Figure 3. It is observed that these SFGs generally have negative  $FUV - NUV$  color gradients (redder centers) and thus have negative dust gradients (more dust extinguished in the centers). A steady increase of negative dust gradient (the slope tends to become steeper) with galaxy mass is also observed.

In Figure 4, we show the profiles of raw dust-reddened  $NUV - B$ , dust-corrected  $NUV - B$  and inferred sSFR in each adopted mass bin, respectively. The shaded regions show the best-fit linear models with  $2\sigma$  lower and upper limits to all individual profiles. The best-fit slopes and intercepts are also presented in Table 1. The dust correction exploits inferred  $A_V$  profiles shown in the bottom panels of Figure 3 and assumes a Calzetti law. sSFR profiles were computed with the  $(NUV - B)_{\text{dc}}$  profiles after applying the calibration shown in the right panel of Figure 2. It can be seen that these SFGs generally have negative  $NUV - B$  color gradients (redder centers), and the color gradients strongly increase with galaxy mass. However, after correcting for dust reddening, the  $NUV - B$  color profiles become nearly flat (the slopes are within  $\pm 0.05$ ), which results in nearly flat sSFR gradients.

To evaluate the PSF effect, the individual rest-frame  $FUV$ ,  $NUV$  and  $B$  band surface brightness profiles in each mass bin are stacked together (taking median values) based on the angular distance in arcsec. We then fit the stacking surface brightness profiles in each band with a single Sérsic model convolving with CANDELS PSF in F160W. The resulting profiles based on PSF-deconvolved Sérsic models in each bin are shown with green dashed lines in Figure 3 and Figure 4, respectively. The slopes and intercepts of the best linear fits to these profiles are listed in Table 1 as well. The same conclusions can be drawn from these PSF-deconvolved data.

#### 5. DISCUSSION AND CONCLUSION

In this Letter, we extend our previous work on the origins of UV-optical color gradients in SFGs at  $z \sim 1$  (Liu et al. 2016) to those at  $z \sim 2$ , using a sample of 1335 main-sequence SFGs with extended UV emission in the mass range  $M_* = 10^9 - 10^{11} M_\odot$  at  $1.5 < z < 2.8$  in the CANDELS/GOODS-S and UDS fields. By fitting reddened stellar population models to the integrated SEDs from observed FUV to NIR, we calibrate  $A_V$  with the rest-frame  $FUV - NUV$  for these SFGs. We demonstrate that rest-frame  $NUV - B$  color is indeed a good tracer of sSFR after correcting for dust reddening. Applying these calibrations to our spatially-resolved data that ends at observed  $H$ , we infer the radial  $A_V$  gradients and sSFR gradients and demonstrate their effects on the  $NUV - B$  color gradients. We find a steady increase of negative dust gradient with galaxy mass. The SFGs generally have negative  $NUV - B$  color gradients, and the color gradients strongly increase with galaxy mass. After correcting for dust gradients, the  $NUV - B$  color profiles become nearly flat regardless of galaxy mass, which indicates that the sSFR gradients are negligibly small. These findings imply that dust reddening is likely the principal cause of negative UV-optical color gradients in these SFGs. The findings support that at  $z \sim 2$  the SFGs buildup their stellar masses in a self-similar way.

Here we compare our results to those of Tacchella et al. (2015, 2017), who explored sSFR gradients in  $z \sim 2.2$  galaxies for a small sample. In Tacchella et al. (2015), they corrected for dust reddening assuming a flat attenuation profile and claimed rather shallow sSFR gradients in low-mass ( $M_* < 10^{11} M_\odot$ ) galaxies but significant sSFR gradients in galaxies with  $M_* \sim 10^{11} M_\odot$ . In Tacchella et al. (2017), they used the  $UV-\beta$  technique to correct for dust reddening and found flat sSFR profiles for  $z \sim 2.2$  galaxies in the mass range  $M_* = 10^{10} - 10^{11} M_\odot$ , which is consistent with our finding. Our finding is also consistent with that from cosmological zoom-in simulations (Tacchella et al. 2016).

If the sSFR profiles appear to be constant with radius at all radii and all times, this would yield SFGs with constant stellar-mass effective radii. In contrast, light-

weighted effective radii are seen to increase roughly as  $M_*^{0.3}$  (e.g., Patel et al. 2013; van Dokkum et al. 2013). It has been known that mass-weighted radii are smaller than light-weighted for SFGs (Szomoru et al. 2013). The discrepancy can also be reconciled if galaxies grow mainly outside  $2R_{\text{SMA}}$  via star formation (Tacchella et al. 2016) or minor mergers (Welker et al. 2017). We leave this problem open because our data only sample the regions inside  $2R_{\text{SMA}}$ .

We note that the *HST* drizzled WFC3 images have the spatial resolution of  $\text{FWHM} \sim 0.18''$  (3 pixels). Therefore, the color gradients in this very central region are missed by this analysis. This is the best that can be done with the present imaging data available. We stress that major conclusions in this paper depend on the SED modeling assumptions applied to the CANDELS data. The majority of our assumptions are single- $\tau$  solar metallicity models and the dust extinction law is assumed to be the Calzetti law. Wang et al. (2017) showed that the dust-reddened radial color variance for the main-sequence SFGs at  $z \sim 1$  run almost parallel to the Calzetti vectors in the *UVI* diagram. But whether the extinction curve of SFGs at  $z \sim 2$  also follows the Calzetti law is still unknown. These assumptions are standard and have been used in all of high- $z$  studies. This paper does not attempt to justify these current state of the art assumptions, but takes the standard assumptions as given and aims to see where they lead to. Future works should investigate the consequences of more realistic stellar population models, metallicity, and extinction law.

We acknowledge the anonymous referee for a constructive report that significantly improved this paper. This work was supported by the National Science Foundation of China (Grant No. 11573017 to FL and No. 11333003, 11390372 to SM). XZ is supported by the National Basic Research Program of China (973 Program 2013CB834900) and the Chinese Academy of Sciences (CAS) through a grant to the CAS South America Center for Astronomy (CASSACA) in Santiago, Chile.

## REFERENCES

- Bertin, E. & Arnouts, S. 1996, *A&AS*, 117, 393
- Brammer, G. B., van Dokkum, P. G., & Coppi, P. 2008, *ApJ*, 686, 1503
- Bruzual, G. & Charlot, S. 2003, *MNRAS*, 344, 1000
- Buat, V., Iglesias-Páramo, J., Seibert, M., et al. 2005, *ApJL*, 619, L51
- Calzetti, D., Armus, L., Bohlin, R. C., et al. 2000, *ApJ*, 533, 682
- Chabrier, G. 2003, *PASP*, 115, 763
- Chary, R. & Elbaz, D. 2001, *ApJ*, 556, 562
- Dahlen, T., Mobasher, B., & Faber, S. M., et al. 2013, *ApJ*, 775, 93

- Galamez, A., Grazian, A., Fontana, A., & the CANDELS Team. 2013, *ApJS*, 206, 10
- Grogin, N. A., Kocevski, D. D., & Faber, S. M., et al. 2011, *ApJS*, 197, 35
- Guo, Y., Ferguson, H. C., & Giavalisco, M., et al. 2013, *ApJS*, 207, 24
- Kaviraj, S., Rey, S.-C., Rich, R. M., et al. 2007, *MNRAS*, 381, L74
- Kennicutt, R. C. & Evans, N. J. 2012, *ARA&A*, 50, 531
- Koekemoer, A. M., Faber, S. M., & Ferguson, H. C., et al. 2011, *ApJS*, 197, 36
- Kriek, M., van Dokkum, P. G., Labbé, I., et al. 2009, *ApJ*, 700, 221
- Laidler, V. G., Papovich, C., & Grogin, N. A., et al. 2007, *PASP*, 119, 1325
- Liu, F. S., Jiang, D., Guo, Y., et al. 2016, *ApJL*, 822, L25
- Morishita, T., Ichikawa, T., Noguchi, M., et al. 2015, *ApJ*, 805, 34
- Muñoz-Mateos, J. C., Gil de Paz, A., Boissier, S., et al. 2007, *ApJ*, 658, 1006
- Nelson, E. J., van Dokkum, P. G., Brammer, G., et al. 2012, *ApJL*, 747, L28
- Nelson, E. J., van Dokkum, P. G., Förster Schreiber, N. M., et al. 2016a, *ApJ*, 828, 27
- Nelson, E. J., van Dokkum, P. G., Momcheva, I. G., et al. 2016b, *ApJL*, 817, L9
- Pan, Z., Li, J., Lin, W., Wang, J., Fan, L., & Kong, X. 2015, *ApJL*, 804, L42
- Patel, S. G., Kelson, D. D., Holden, B. P., Franx, M., & Illingworth, G. D. 2011, *ApJ*, 735, 53
- Patel, S. G., van Dokkum, P. G., Franx, M., et al. 2013, *ApJ*, 766, 15
- Peng, C. Y., Ho, L. C., Impey, C. D., & Rix, H.-W. 2002, *AJ*, 124, 266
- Reddy, N., Dickinson, M., Elbaz, D., et al. 2012, *ApJ*, 744, 154
- Salim, S., Dickinson, M., Michael Rich, R., et al. 2009, *ApJ*, 700, 161
- Santini, P., Ferguson, H. C., & Fontana, A., et al. 2015, *ApJ*, 801, 97
- Szomoru, D., Franx, M., van Dokkum, P. G., et al. 2013, *ApJ*, 763, 73
- Tacchella, S., Carollo, C. M., Renzini, A., et al. 2015, *Science*, 348, 314
- Tacchella, S., Dekel, A., Carollo, C. M., et al. 2016, *MNRAS*, 458, 242
- Tacchella, S., Carollo, C. M., Förster Schreiber, N. M., et al. 2017, *Arxiv e-print (arXiv:1704.00733)*
- Tielens, A. G. G. M. 2008, *ARA&A*, 46, 289
- van der Wel, A., Bell, E. F., & Häussler, B., et al. 2012, *ApJS*, 203, 24
- van der Wel, A., Franx, M., van Dokkum, P. G., et al. 2014, *ApJ*, 788, 28
- van Dokkum, P. G., Leja, J., Nelson, E. J., et al. 2013, *ApJL*, 771, L35
- Wang, W., Faber, S. M., Liu, F. S., et al. 2017, *ArXiv e-prints (arXiv:1705.05404)*
- Welker, C., Dubois, Y., Devriendt, J., et al. 2017, *MNRAS*, 465, 1241
- Whitaker, K. E., Franx, M., & Leja, J., et al. 2014, *ApJ*, 795, 104
- Whitaker, K. E., Kriek, M., van Dokkum, P. G., et al. 2012, *ApJ*, 745, 179
- Williams, R. J., Quadri, R. F., Franx, M., van Dokkum, P., & Labbé, I. 2009, *ApJ*, 691, 1879
- Wuyts, S., Förster Schreiber, N. M., Genzel, R., et al. 2012, *ApJ*, 753, 114

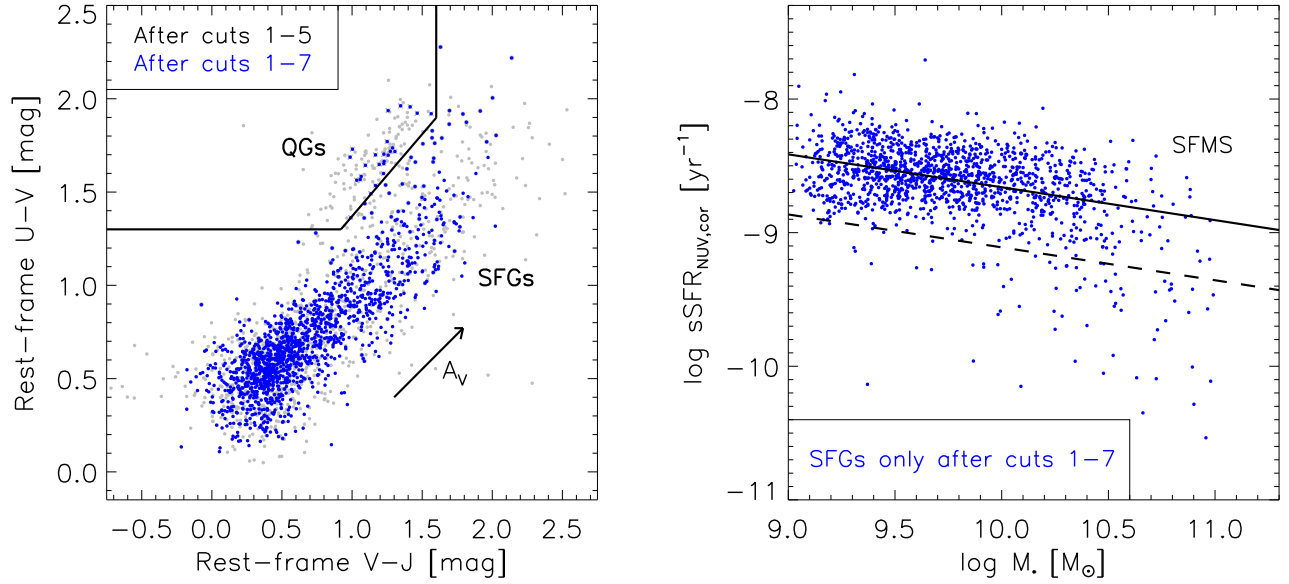


**Figure 1.** Left panel: Rest-frame global  $UVJ$  diagram for the parent samples after applying the selection cuts 1-5 and 1-7 (see §1), respectively. The solid lines indicate the classification criterion provided by Williams et al. (2009). The arrow shows the Calzetti vector. Right panel:  $sSFR$  vs. stellar mass for only  $UVJ$ -defined SFGs after the cuts 1-7. The solid line shows the best-fit linear relation to the SFMS. The transition galaxies, defined to have residuals  $\Delta \log sSFR_{NUV,cor} < -0.45$  dex (below the dashed line), are excluded in this analysis.

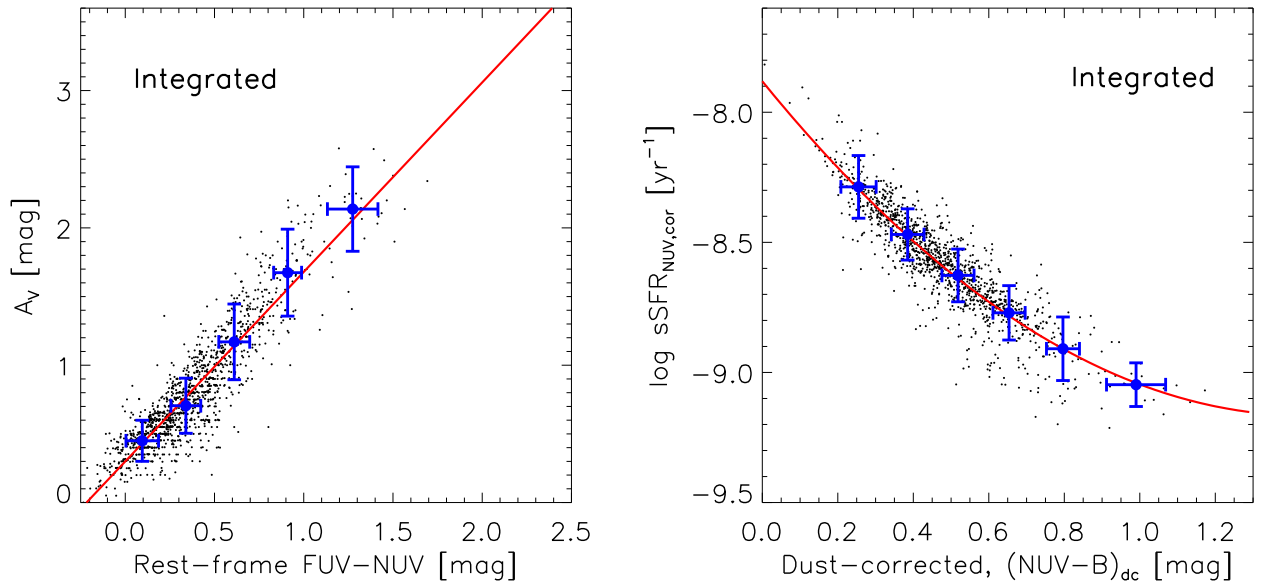


**Figure 2.** Correlations of  $A_V$  versus  $FUV - NUV$  (left) and  $\log sSFR_{NUV,cor}$  versus  $(NUV - B)_{dc}$  (right) for global (integrated) SFGs. The red line in the left panel is the best linear fit to the relation. The red line in the right panel is the best polynomial fit to the relation. The two plots will be used as calibrations to infer dust and  $sSFR$  radial profiles of the galaxies in this study.

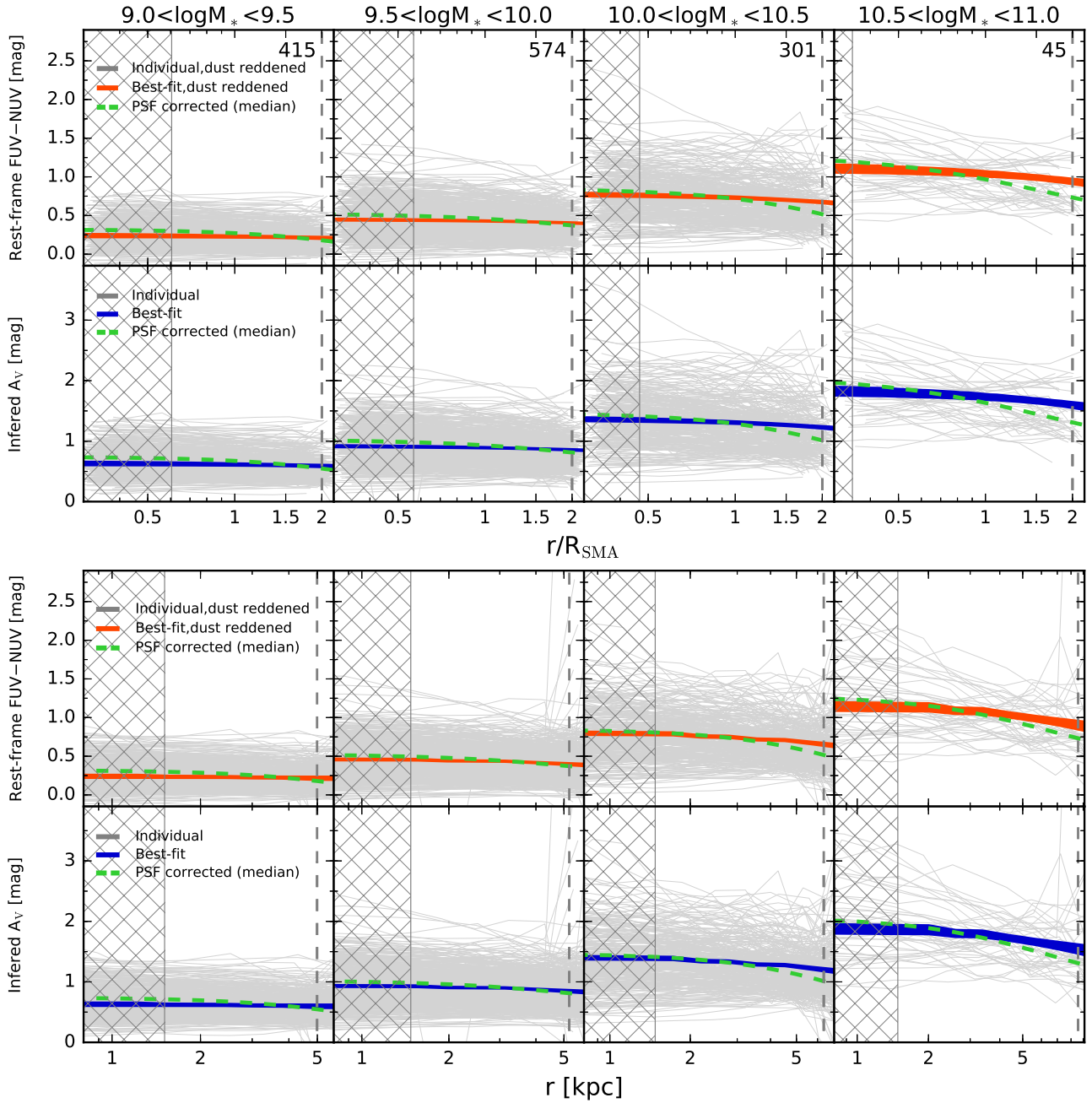


**Figure 3.** Rest-frame dust-reddened  $FUV - NUV$  profiles and inferred  $A_V$  profiles in each mass bin, which are normalised by their  $R_{SMA}$  in arcsec (upper) and are shown in physical radius (lower), respectively. The individual profiles are shown with gray lines. The shade regions show the best-fit linear models with  $2\sigma$  lower and upper limits to all individual profiles (no PSF-correction). The green dashed lines are PSF-corrected median profiles. The gray grids indicate the regions within the median values of twice the PSF radius ( $0.18''$ ). The vertical dashed lines indicate the positions of  $2R_{SMA}$  (median values for the profiles in kpc).



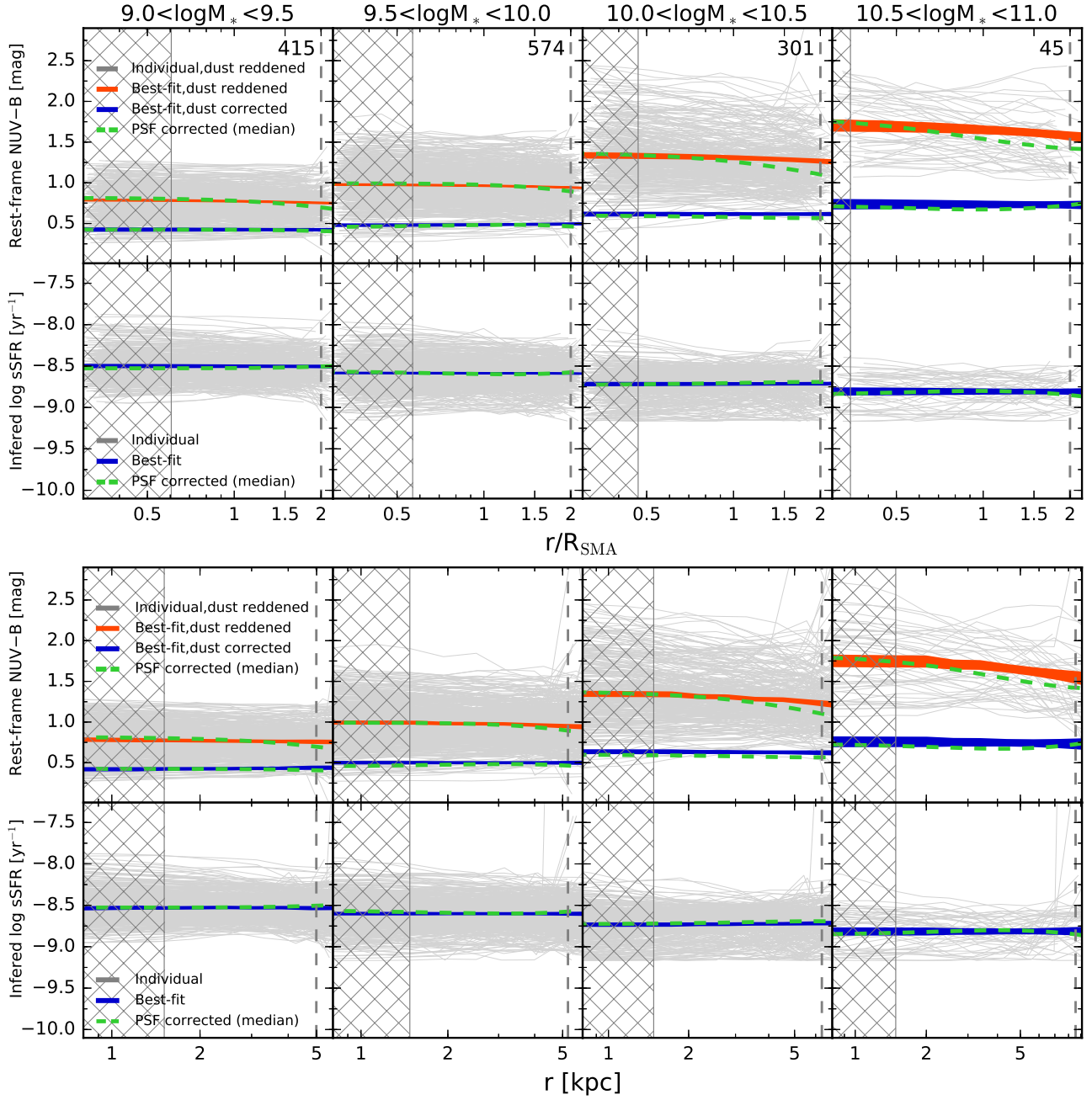


**Figure 4.** Rest-frame  $NUV - B$  profiles (both dust-reddened and dust-corrected) and inferred sSFR profiles in each mass bin, which are normalised by their  $R_{SMA}$  in arcsec (upper) and are shown in physical radius (lower), respectively. Only the individual galaxy profiles are shown with gray lines for dust-reddened  $NUV - B$  and inferred sSFR. The shade regions show the best-fit linear models with  $2\sigma$  lower and upper limits to all individual profiles (no PSF-correction). The green dashed lines are PSF-corrected median profiles. The gray grids indicate the regions within the median values of twice the PSF radius ( $0.18''$ ). The vertical dashed lines indicate the positions of  $2R_{SMA}$  (median values for the profiles in kpc).

Table 1. Parameters of the best-fit linear models to our profiles

Contents	9.0 < logM* < 9.5		9.5 < logM* < 10.0		10.0 < logM* < 10.5		10.5 < logM* < 11.0	
	Slope	Intercept	Slope	Intercept	Slope	Intercept	Slope	Intercept
Profiles scaled by $R_{SMA}$ in arcsec (no PSF-correction)								
FUV-NUV	-0.104±0.045	0.223±0.007	-0.141±0.025	0.420±0.004	-0.273±0.040	0.697±0.007	-0.390±0.074	0.960±0.017
$A_V$	-0.143±0.062	0.607±0.010	-0.195±0.035	0.879±0.006	-0.377±0.055	1.261±0.010	-0.538±0.102	1.624±0.024
NUV-B	-0.069±0.006	0.753±0.019	-0.071±0.005	0.942±0.001	-0.199±0.045	1.284±0.008	-0.303±0.087	1.590±0.020
(NUV-B) <sub>dc</sub>	-0.008±0.029	0.424±0.005	0.049±0.019	0.488±0.003	0.000±0.030	0.615±0.005	-0.018±0.072	0.730±0.017
log sSFR	-0.017±0.029	-8.503±0.004	-0.012±0.004	-8.590±0.001	0.013±0.025	-8.714±0.005	-0.004±0.052	-8.808±0.012
Profiles in kpc (no PSF-correction)								
FUV-NUV	-0.073±0.052	0.261±0.024	-0.167±0.029	0.503±0.013	-0.350±0.040	0.891±0.021	-0.447±0.085	1.263±0.049
$A_V$	-0.101±0.071	0.659±0.034	-0.231±0.040	0.993±0.018	-0.482±0.055	1.528±0.029	-0.617±0.117	2.041±0.068
NUV-B	-0.003±0.036	0.753±0.017	-0.126±0.031	1.028±0.014	-0.286±0.047	1.454±0.024	-0.374±0.096	1.852±0.056
(NUV-B) <sub>dc</sub>	0.046±0.034	0.403±0.016	-0.004±0.022	0.502±0.010	-0.031±0.033	0.644±0.017	-0.048±0.080	0.770±0.047
log sSFR	-0.044±0.033	-8.466±0.016	-0.004±0.023	-8.600±0.011	0.042±0.027	-8.745±0.014	0.007±0.056	-8.818±0.033
PSF-corrected stacking profiles scaled by $R_{SMA}$ in arcsec								
FUV-NUV	-0.214±0.021	0.263±0.004	-0.252±0.013	0.454±0.002	-0.446±0.037	0.693±0.007	-0.686±0.019	0.954±0.004
$A_V$	-0.296±0.029	0.662±0.005	-0.348±0.017	0.926±0.003	-0.616±0.051	1.256±0.010	-0.946±0.026	1.615±0.005
NUV-B	-0.184±0.021	0.772±0.003	-0.197±0.024	0.971±0.004	-0.373±0.027	1.243±0.005	-0.457±0.009	1.543±0.002
(NUV-B) <sub>dc</sub>	-0.028±0.005	0.421±0.001	-0.013±0.015	0.480±0.002	-0.046±0.002	0.577±0.000	0.045±0.020	0.688±0.004
log sSFR	0.035±0.006	-8.522±0.001	0.015±0.018	-8.594±0.003	0.050±0.002	-8.705±0.000	-0.041±0.019	-8.815±0.004
PSF-corrected stacking profiles in kpc								
FUV-NUV	-0.214±0.021	0.348±0.010	-0.223±0.015	0.543±0.008	-0.511±0.034	0.957±0.020	-0.686±0.019	1.387±0.013
$A_V$	-0.296±0.029	0.780±0.014	-0.308±0.021	1.048±0.010	-0.705±0.047	1.620±0.028	-0.946±0.026	2.213±0.018
NUV-B	-0.184±0.021	0.845±0.010	-0.187±0.023	1.030±0.012	-0.422±0.024	1.460±0.014	-0.457±0.009	1.832±0.006
(NUV-B) <sub>dc</sub>	-0.028±0.005	0.432±0.002	0.006±0.013	0.475±0.006	-0.048±0.002	0.602±0.001	0.045±0.020	0.659±0.014
log sSFR	0.035±0.006	-8.536±0.003	-0.007±0.015	-8.588±0.008	0.049±0.002	-8.730±0.001	-0.041±0.019	-8.789±0.013